

GS-SLAM: Dense Visual SLAM with 3D Gaussian Splatting

Chi Yan^{1*} Delin Qu^{1,2*} Dong Wang¹ Dan Xu⁴
 Zhigang Wang¹ Bin Zhao^{1,3} Xuelong Li^{1,3}
¹Shanghai AI Laboratory ²Fudan University ³Northwestern Polytechnical University
⁴The Hong Kong University of Science and Technology

Abstract

In this paper, we introduce **GS-SLAM** that first utilizes 3D Gaussian representation in the Simultaneous Localization and Mapping (SLAM) system. It facilitates a better balance between efficiency and accuracy. Compared to recent SLAM methods employing neural implicit representations, our method utilizes a real-time differentiable splatting rendering pipeline that offers significant speedup to map optimization and RGB-D re-rendering. Specifically, we propose an adaptive expansion strategy that adds new or deletes noisy 3D Gaussian in order to efficiently reconstruct new observed scene geometry and improve the mapping of previously observed areas. This strategy is essential to extend 3D Gaussian representation to reconstruct the whole scene rather than synthesize a static object in existing methods. Moreover, in the pose tracking process, an effective coarse-to-fine technique is designed to select reliable 3D Gaussian representations to optimize camera pose, resulting in runtime reduction and robust estimation. Our method achieves competitive performance compared with existing state-of-the-art real-time methods on the Replica, TUM-RGBD datasets. The source code will be released upon acceptance.

1. Introduction

Simultaneous localization and mapping (SLAM) has emerged as a pivotal technology in fields such as robotics [5], virtual reality [8], and augmented reality [20, 34]. The goal of SLAM is to construct a dense/sparse map of an unknown environment while simultaneously tracking the camera pose. Traditional SLAM methods employ point/surfel clouds [16, 27, 36, 40], mesh representations [21], voxel hashing [10, 14, 19] or voxel grids [17] as scene representations to construct dense mapping, and have made considerable progress on localization accuracy. However, these methods face serious challenges in obtaining fine-grained dense maps.

Recently, Neural Radiance Fields (NeRF) [15] have

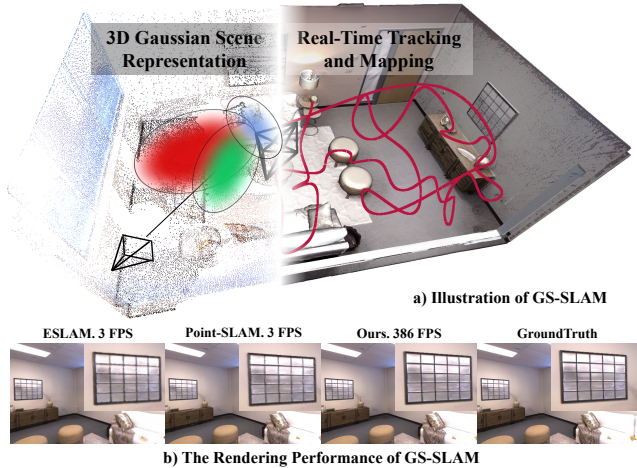


Figure 1. The illustration of the proposed GS-SLAM. It first utilizes the 3D Gaussian representation and differentiable splatting rasterization pipeline in SLAM, achieving real-time tracking and mapping performance on GPU. Besides, benefiting from the splatting rasterization pipeline, GS-SLAM achieves a 100× faster rendering FPS and more high-quality full image results than the other SOTA methods.

been explored to enhance SLAM methodologies and exhibit strengths in generating high-quality, dense maps with low memory consumption [30]. In particular, iMAP [30] uses a single multi-layer perceptron (MLP) to represent the entire scene, which is updated globally with the loss between volume-rendered RGB-D image and ground-truth observations. NICE-SLAM [48] utilizes a hierarchical neural implicit grid as scene map representation to allow local updates for reconstructing large scenes.

Moreover, ESLAM [9] and Co-SLAM [35] utilize axis-aligned feature planes and joint coordinate-parametric encoding to improve the capability of scene representation, achieving efficient and high-quality surface map reconstruction. In practical mapping and tracking steps, these methods only render a small set of pixels to reduce optimization time, which leads to the reconstructed dense maps lacking the richness and intricacy of details. In essence, it is

a trade-off for the efficiency and accuracy of NeRF-based SLAM since obtaining high-resolution images with the ray-based volume rendering technique is time-consuming and unacceptable. Fortunately, recent work [11, 13, 41] with 3D Gaussian representation and tile-based splatting techniques has shown great superiority in the efficiency of high-resolution image rendering. It is applied to synthesize novel view RGB images of static objects, achieving state-of-the-art visual quality for 1080p resolution at real-time speed. Inspired by this, we extend the rendering superiority of 3D Gaussian scene representation and real-time differentiable splatting rendering pipeline for the task of dense RGB-D SLAM and manage to jointly promote the speed and accuracy of NeRF-based dense SLAM, as shown in Fig. 1.

To this end, we propose GS-SLAM, the first RGB-D dense SLAM that utilizes 3D Gaussian scene representation coupled with the splatting rendering technique to achieve a better balance between speed and accuracy. Specifically, we first derive an analytical formulation for optimizing camera pose tracking and dense mapping with RGB-D re-rendering loss, which achieves a fast and accurate backward by sorting and α -blending overlapped 3D Gaussians. For mapping, we propose an adaptive expansion strategy to add new or delete noisy 3D Gaussian representations to efficiently reconstruct new observed scene geometry while improving the mapping of the previously observed areas. This strategy makes every mapping step optimize the currently visible and correct 3D Gaussian representations rather than irrelevant ones from previously observed areas, significantly improving the mapping effectiveness and reducing artifacts in reconstructed dense maps and rendered images. In camera tracking process, an effective coarse-to-fine technique is designed to first estimate coarse camera pose using the loss of re-rendered low-resolution images, then a set of reliable 3D Gaussian scene representations are selected to refine camera pose by re-rendering high-resolution images, resulting in the running time reduction and performance promotion. We perform extensive evaluations on a selection of indoor RGB-D datasets and demonstrate state-of-the-art performance on dense neural RGB-D SLAM in terms of tracking, rendering, and mapping. Overall, our contributions include:

- We propose GS-SLAM, the first 3D Gaussian-based dense RGB-D SLAM approach, which takes advantage of the fast splatting rendering technique to boost the mapping optimizing and pose tracking, achieving real-time and photo-realistic reconstruction performance.
- We present an adaptive 3D Gaussians expansion strategy to efficiently reconstruct new observed scene geometry and develop a coarse-to-fine technique to select reliable 3D Gaussians to improve camera pose estimation.
- Our approach achieves competitive performance on Replica and TUM-RGBD datasets in terms of tracking,

mapping and runs at 8.43 FPS, resulting in a better balance between efficiency and accuracy.

2. Related Work

Dense Visual SLAM. The existing real-time dense visual SLAM systems are typically based on discrete handcrafted features or deep-learning embeddings, and follow the mapping and tracking architecture in [12]. DTAM [18] first introduces a dense SLAM system that uses photometric consistency to track a handheld camera and represent the scene as a cost volume. KinectFusion [38] performs camera tracking by iterative-closest-point and updates the scene via TSDF-Fusion. BAD-SLAM [24] proposes to jointly optimize the keyframe poses and 3D scene geometry via a direct bundle adjustment (BA) technique. In contrast, recent works integrate deep learning with the traditional geometry framework for more accurate and robust camera tracking and mapping, such as DROID-SLAM [32], CodeSLAM [1], SceneCode [47], and NodeSLAM [29], have made significant advances in the field, achieving more accurate and robust camera tracking and mapping performance.

Neural Implicit Radiance Field based SLAM. For NeRF-based SLAM, existing methods can be divided into three main types: *MLP-based methods*, *Hybrid representation methods*, and *Explicit methods*. MLP-based method iMAP [30] offers scalable and memory-efficient map representations but faces challenges with catastrophic forgetting in larger scenes. Hybrid representation methods combine the advantages of implicit MLPs and structure features, significantly enhancing the scene scalability and precision. For example, NICE-SLAM [48] integrates MLPs with multi-resolution voxel grids, enabling large scene reconstruction, and Vox-Fusion [42] employs octree expansion for dynamic map scalability, while ESLAM [9] and Point-SLAM [22] utilize tri-planes and neural point clouds respectively to improve the mapping capability. As for the explicit method proposed in [33], it stores map features in voxel directly, without any MLPs, enabling a faster optimization. Instead of representing maps with implicit features, GS-SLAM utilizes the 3D Gaussian representation, efficiently renders images using splatting-based rasterization, and optimizes parameters directly with backward propagation.

3D Gaussians Representation. Gaussian splatting demonstrates great superiorities in high-quality real-time novel-view synthesis. The work proposed in [11] first introduces to represent the scene with 3D Gaussian and develops a fast rendering algorithm to support anisotropic splatting, achieving SOTA visual quality and fast high-resolution rendering performance. Beyond the rendering superiorities, Gaussian splatting holds an explicit geometry scene structure and appearance, benefiting from the exact modeling of scenes representation [44]. This promising technology has

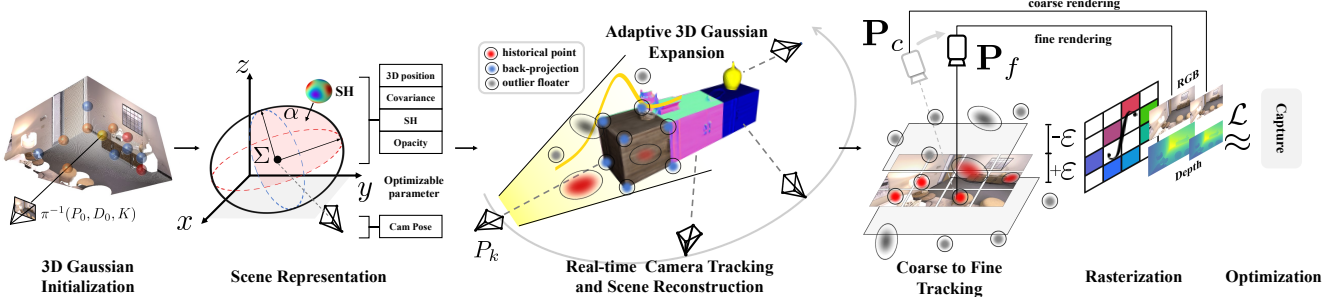


Figure 2. Overview of the proposed method. We aim to use 3D Gaussian to represent the scene and use the rendered RGB-D image for inverse camera tracking. GS-SLAM proposes a novel Gaussian expansion strategy to make the 3D Gaussian feasible to reconstruct the whole scene and can achieve real-time tracking, mapping, and rendering performance on GPU.

been rapidly applied in several fields, including 3D generation [3, 31, 45], dynamic scene modeling [13][41][43], and photorealistic drivable avatars [49]. However, currently, there is no research addressing camera pose estimation or real-time mapping using 3D Gaussian models due to the inherent limitations of the prime pipeline [11], *i.e.*, prerequisites of initialized point clouds or camera pose inputs [23]. In contrast, we derive the analytical derivative equations for pose estimation in the Gaussian representation and implement efficient CUDA optimization.

3. Methodology

Fig. 2 shows the overview of the proposed GS-SLAM. We aim to estimate the camera poses of every frame $\{\mathbf{P}_i\}_{i=1}^N$ and simultaneously reconstruct a dense scene map by giving an input sequential RGB-D stream $\{\mathbf{I}_i, \mathbf{D}_i\}_{i=1}^M$ with known camera intrinsic $\mathbf{K} \in \mathbb{R}^{3 \times 3}$. In Sec. 3.1, we first introduce 3D Gaussian as the scene representation \mathbf{S} and the RGB-D render by differentiable splatting rasterization. With the estimated camera pose of the keyframe, in Sec. 3.2, an adaptive expansion strategy is proposed to add new or delete noisy 3D Gaussian representations to efficiently reconstruct new observed scene geometry while improving the mapping of the previously observed areas. For camera tracking of every input frame, we derive an analytical formula for backward optimization with re-rendering RGB-D loss, and further introduce an effective coarse-to-fine technique to minimize re-rendering losses to achieve efficient and accurate pose estimation in Sec. 3.3.

3.1. 3D Gaussian Scene Representation

Our goal is to optimize a scene representation that captures geometry and appearance of the scene, resulting in detailed dense map and high-quality novel view synthesis. To do this, we model the scene as a set of 3D Gaussian coupled with opacity and spherical harmonics

$$\mathbf{G} = \{G_i : (\mathbf{X}_i, \Sigma_i, \Lambda_i, \mathbf{Y}_i) | i = 1, \dots, N\}. \quad (1)$$

Each 3D Gaussian scene representation G_i is defined by position $\mathbf{X}_i \in \mathbb{R}^3$, 3D covariance matrix $\Sigma_i \in \mathbb{R}^{3 \times 3}$, opacity $\Lambda_i \in \mathbb{R}$ and 1 degree Spherical Harmonics (\mathbf{Y}) per color channel, total of 12 coefficients for $\mathbf{Y}_i \in \mathbb{R}^{12}$. In order to reduce the learning difficulty of the 3D Gaussians [50], we parameterize the 3D Gaussian covariance as:

$$\Sigma = \mathbf{R}\mathbf{S}\mathbf{S}^T\mathbf{R}^T, \quad (2)$$

where $\mathbf{S} \in \mathbb{R}^3$ is a 3D scale vector, $\mathbf{R} \in \mathbb{R}^{3 \times 3}$ is rotation matrix, storing as a 4D quaternion.

Color and Depth Splatting Rendering. With the optimized 3D Gaussian scene representation parameters, given the camera pose $\mathbf{P} = \{\mathbf{R}, \mathbf{t}\}$, the 3D Gaussians G are projected into 2D image plane for rendering with:

$$\Sigma' = \mathbf{J}\mathbf{P}^{-1}\Sigma\mathbf{P}^{-T}\mathbf{J}^T, \quad (3)$$

where \mathbf{J} is the Jacobian of the affine approximation of the projective function. After projecting 3D Gaussians to the image plane, the color of one pixel is rendered by sorting the Gaussians in depth order and performing front-to-back α -blending rendering as follows:

$$\hat{\mathbf{C}} = \sum_{i \in N} \mathbf{c}_i \alpha_i \prod_{j=1}^{i-1} (1 - \alpha_j), \quad (4)$$

where \mathbf{c}_i represents color of this Gaussian obtained by learned \mathbf{Y} Spherical Harmonics coefficients, α_i is the density computed by multiplying 2D covariance Σ' with opacity Λ_i . Similarly, the depth is rendered by

$$\hat{D} = \sum_{i \in N} d_i \alpha_i \prod_{j=1}^{i-1} (1 - \alpha_j), \quad (5)$$

where d_i denotes the depth of the center of the i -th 3D Gaussian, which is obtained by projecting to z-axis in the camera coordinate system.

3.2. Adaptive 3D Gaussian Expanding Mapping

The 3D Gaussian scene representations are updated and optimized on each selected keyframe for stable mapping. Given the estimated pose of each selected keyframes, we first apply the proposed adaptive expansion strategy to add new or delete noisy 3D Gaussians from the whole scene representations to render RGB-D images with resolution $H \times W$, and then the updated 3D Gaussian scene representations are optimized by minimizing the geometric depth loss \mathcal{L}_d and the photometric color loss \mathcal{L}_c to the sensor observation depth D and color \mathbf{C} ,

$$\mathcal{L}_c = \sum_{m=1}^{HW} |\mathbf{C}_m - \hat{\mathbf{C}}_m|, \quad \mathcal{L}_d = \sum_{m=1}^{HW} |D_m - \hat{D}_m|. \quad (6)$$

The loss optimizes the parameters of all 3D Gaussians that contribute to the re-rendering of these keyframe images.

Adaptive 3D Gaussian Expansion Strategy. At the first frame of the RGB-D sequence, we first uniformly sample half pixels from a whole image with $H \times W$ resolution and back-projecting them into 3D points \mathbf{X} with corresponding depth observation D . The 3D Gaussian scene representations are created by setting position as \mathbf{X} and initializing zero degree \mathbf{Y} coefficients with RGB color \mathbf{C}_i . The opacities are set to pre-defined values, and the covariance is set depending on the spatial point density, *i.e.*,

$$\{G_i = (\mathbf{P}_i, \Sigma_{init}, \Lambda_{init}, \mathbf{C}_i) | i = 1, \dots, M\}, \quad (7)$$

where M equals to $HW/2$. This initialized scene representation is optimized with re-rendering loss on the first RGB-D image. Note that only half of the pixels are used to initialize the scene, leaving space to conduct adaptive density control of Gaussians that splits large points into smaller ones and clones them with different directions to capture missing geometric details.

Adding Step: to obtain a complete map of the environment, the 3D Gaussian scene representations should be able to model the geometry and appearance of newly observed areas. Specifically, at every keyframe, we add first re-render RGB-D images using historical 3D Gaussian scene representations and calculate cumulative opacity $T = \sum_{i \in N} \alpha_i \prod_{j=1}^{i-1} (1 - \alpha_j)$ for each pixel. We label one pixel as un-reliable x^{un} if its cumulative opacity T is too low or its re-rendering depth \hat{D} is far away from observed depth D , *i.e.*,

$$T < \tau_T \quad \text{or} \quad |D - \hat{D}| > \tau_D. \quad (8)$$

These selected un-reliable pixels mostly capture new observed areas. Then we back-project these un-reliable pixels to 3D points \mathbf{P}^{un} , and a set of new 3D Gaussians at \mathbf{P}^{un} initialized as Eq. 7 are added into scene representations to model the new observed areas.

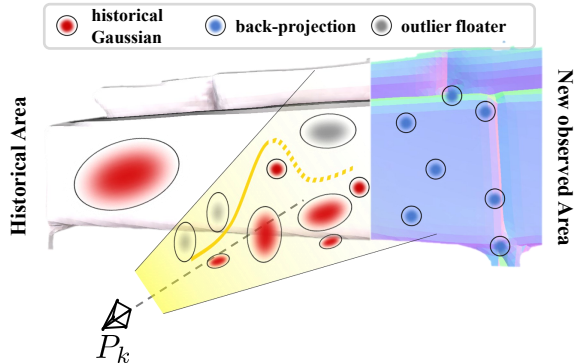


Figure 3. Illustration of the proposed adaptive 3D Gaussian expansion strategy. GS-SLAM inhibits the low-quality 3D Gaussian floaters in the current frustum according to depth.

Deleting Step: as shown in Fig. 3, there are some floating 3D Gaussians due to the unstable adaptive control of Gaussians after optimization with Eq. 6. These floating 3D Gaussians will result in a low-quality dense map and a re-rendered image containing lots of artifacts. To address this issue, after adding new 3D Gaussians, we check all visible 3D Gaussians in the current camera frustum and significantly decrease opacity Λ_i of 3D Gaussians whose position is not near the scene surfaces. Formally, for each visible 3D Gaussian, we draw a ray $\mathbf{r}(t)$ from camera origin \mathbf{o} and its position $\mathbf{X}_i = (x_i, y_i, z_i)$, *i.e.*, $\mathbf{r}(t) = \mathbf{o} + t(\mathbf{X}_i - \mathbf{o})$. Then, we can find a pixel with coordinate (u, v) where this ray intersects image plane and corresponding depth observation D . The 3D Gaussians are deleted by degenerating its opacity as follows:

$$G_i : \Lambda_i \Rightarrow G_i : \eta \Lambda_i, \quad \text{if } D - \text{dist}(\mathbf{X}_i, \mathbf{P}_{uv}) > \gamma, \quad (9)$$

where \mathbf{P}_{uv} is the world coordinates of the intersected pixel calculated with the camera intrinsic and extrinsic. $\text{dist}(\cdot, \cdot)$ is the Euclidean distance, and η (much smaller than 1) and γ are the hyperparameters. Note that we decrease the opacity of floating 3D Gaussians in front of the scene surfaces to make our newly added 3D Gaussians well-optimized.

3.3. Tracking and Bundle Adjustment

In the parallel camera tracking phase of our work, we first employ a common straightforward constant velocity assumption to initialize new poses. This assumption transforms the last known pose based on the relative transformation between the second-to-last pose and the last pose. Then, the accurate camera pose \mathbf{P} is optimized by minimizing re-rendering color loss, *i.e.*,

$$\mathcal{L}_{track} = \sum_{m=1}^M |\mathbf{C}_m - \hat{\mathbf{C}}_m|_1, \quad \min_{\mathbf{R}, \mathbf{t}}(\mathcal{L}_{track}), \quad (10)$$

where M is the number of sampled pixels for re-rendering.

Differentiable Pose Estimation. According to Eqs. (3) and (4), we observe that the gradient of the camera pose \mathbf{P} is related to three intermediate variables: Σ' , \mathbf{c}_i and the projected coordinate \mathbf{m}_i of Gaussian G_i . By applying the chain rule of derivation, we obtain the analytical formulation of camera pose \mathbf{P} :

$$\begin{aligned} \frac{d\mathcal{L}_c}{d\mathbf{P}} &= \frac{d\mathcal{L}_c}{d\mathbf{C}} \frac{d\mathbf{C}}{d\mathbf{P}} = \frac{d\mathcal{L}_c}{d\mathbf{C}} \left(\frac{d\mathbf{C}}{dc_i} \frac{dc_i}{d\mathbf{P}} + \frac{d\mathbf{C}}{d\alpha_i} \frac{d\alpha_i}{d\mathbf{P}} \right) \\ &= \frac{d\mathcal{L}_c}{d\mathbf{C}} \frac{d\mathbf{C}}{d\alpha_i} \left(\frac{d\alpha_i}{d\Sigma'} \frac{d\Sigma'}{d\mathbf{P}} + \frac{d\alpha_i}{d\mathbf{m}_i} \frac{d\mathbf{m}_i}{d\mathbf{P}} \right), \quad (11) \\ &= \frac{d\mathcal{L}_c}{d\mathbf{C}} \frac{d\mathbf{C}}{d\alpha_i} \left(\frac{d\alpha_i}{d\Sigma'} \frac{d(\mathbf{J}\mathbf{P}^{-1}\Sigma\mathbf{P}^{-T}\mathbf{J}^T)}{d\mathbf{P}} + \frac{d(\mathbf{K}\mathbf{P}\mathbf{X}_i)}{d\mathbf{P}D_i} \right) \end{aligned}$$

where D_i denotes the z-axis coordinate of projection \mathbf{m}_i . The item $\frac{d\mathbf{C}}{dc_i} \frac{dc_i}{d\mathbf{P}}$ can be eliminated because we only concern about the view-independent color in our tracking implementation. In addition, we find that the intermediate gradient $\frac{d(\mathbf{K}\mathbf{P}\mathbf{X}_i)}{d\mathbf{P}D_i}$ is the deterministic component for the camera pose \mathbf{P} . So we simply ignore the backpropagation of $\frac{d(\mathbf{J}\mathbf{P}^{-1}\Sigma\mathbf{P}^{-T}\mathbf{J}^T)}{d\mathbf{P}}$ for efficiency. More details can be found in the supplemental materials.

Coarse-to-Fine Camera Tracking. Re-rendering and optimizing camera pose with all image pixels would be problematic since artifacts in images will cause a drifted camera tracking. To address this issue, as shown in Fig. 2, in the differentiable pose estimation step for each frame, we first take advantage of image regularity to render only a sparse set of pixels and optimize tracking loss to obtain a coarse camera pose. This coarse optimization step significantly eases the influence of detailed artifacts. Further, we use this coarse camera pose and depth observation to select reliable 3D Gaussians, which guides GS-SLAM to re-render informative areas with clear geometric structures to refine coarse camera pose via further optimizing tracking loss on new rendering pixels.

Specifically, in the coarse stage, we first render a coarse image $\hat{\mathbf{I}}_c$ with resolution $H/2 \times W/2$ at uniformly sampled image coordinates and optimize tracking loss in Eq. 10 for T_c iterations, and the obtained camera pose is denoted as \mathbf{P}_c . In the fine stage, we use a similar technique with adaptive 3D Gaussian expansion strategy in Section 3.2 to select reliable 3D Gaussian to re-render full-resolution images while ignoring noisy 3D Gaussians that cause artifacts. In detail, we check all visible 3D Gaussians under coarse camera pose \mathbf{P}_c , and remove 3D Gaussians whose position is far away to the scene surface. Formally, for each visible 3D Gaussians G_i with position \mathbf{X}_i , we project it to 2D image plane using coarse camera pose \mathbf{P}_c and camera intrinsics. Given the projected pixel’s depth observation D_i and the distance d_i that is between 3D Gaussians G_i and the camera image plane, the reliable 3D Gaussians are se-

lected as follows:

$$\begin{aligned} \mathbf{G}_{selected} &= \{G_i | G_i \in \mathbf{G} \text{ and } abs(D_i - d_i) \leq \varepsilon\}, \\ \hat{\mathbf{I}}_f &= \mathcal{F}(u, v, \mathbf{G}_{selected}), \end{aligned} \quad (12)$$

where we use the selected reliable 3D Gaussians to re-render full resolution images $\hat{\mathbf{I}}_f$. u, v denote the pixel coordinates in $\hat{\mathbf{I}}_f$, and \mathcal{F} represent color splatting rendering function. The final camera poses \mathbf{P} is obtained by optimizing tracking loss in Eq. 10 with $\hat{\mathbf{I}}_f$ for another T_f iterations. Note that $\hat{\mathbf{I}}_c$ and $\hat{\mathbf{I}}_f$ are only re-rendered at previously observed areas, avoiding rendering areas where 3D scene representations have not been optimized in the mapping process. Also, we add keyframes based on the proportion of the currently observed image’s reliable region to the overall image. At the same time, when the current tracking frame and most recent keyframe differ by more than a threshold value μ_k , this frame will be inserted as a keyframe.

Bundle Adjustment. In the bundle adjustment (BA) phase, we optimize the camera poses \mathbf{P} and the 3D Gaussian scene representation \mathbf{S} jointly. We randomly select K keyframes from the keyframe database for optimization, using the loss function similar to the mapping part. For pose optimization stability, we only optimize the scene representation \mathbf{S} in the first half of the iterations. In the other half of the iterations, we simultaneously optimize the map and the poses. Then, the accurate camera pose \mathbf{P} is optimized by minimizing re-rendering color loss, *i.e.*,

$$\mathcal{L}_{ba} = \frac{1}{K} \sum_{k=1}^K \sum_{m=1}^{HW} |D_m - \hat{D}_m|_1 + \lambda_m |C_m - \hat{C}_m|_1, \min_{\mathbf{R}, \mathbf{t}, \mathbf{S}} (\mathcal{L}_{ba}). \quad (13)$$

4. Experiment

4.1. Experimental Setup

Dataset. To evaluate the performance of GS-SLAM, we conduct experiments on the Replica [26], and TUM-RGBD [28]. Following [9, 22, 35, 42, 48], we use 8 scenes from the Replica dataset for localization, mesh reconstruction, and rendering quality comparison. The selected three subsets of TUM-RGBD datasets are used for localization.

Baselines. We compare our method with the existing state-of-the-art NeRF-based dense visual SLAM: iMAP [30], NICE-SLAM [48], Vox-Fusion [42], CoSLAM [35], ES-LAM [9] and Point-SLAM [22]. The rendering performance of CoSLAM [35] and ESLAM [9] is conducted from the open source code with the same configuration in [22].

Metric. For mesh reconstruction, we use the 2D Depth L1 (cm) [48], the Precision (P, %), Recall (R, %), and F-score with a threshold of 1 cm to measure the scene geometry. For localization, we use the absolute trajectory (ATE, cm) error [28] to measure the accuracy of the estimated camera poses. We further evaluate the rendering performance using the peak signal-to-noise ratio (PSNR), SSIM [37] and

Table 1. Tracking comparison (ATE RMSE [cm]) of the proposed method vs. the state-of-the-art methods on **Replica** dataset. The running speed of methods in upper part is lower than 5 FPS, * denotes the reproduced results by running officially released code.

Method	Rm0	Rm1	Rm2	Off0	Off1	Off2	Off3	Off4	avg
Point-SLAM [22]	0.56	0.47	0.30	0.35	0.62	0.55	0.72	0.73	0.54
NICE-SLAM [48]	0.97	1.31	1.07	0.88	1.00	1.06	1.10	1.13	1.06
Vox-Fusion* [42]	1.37	4.70	1.47	8.48	2.04	2.58	1.11	2.94	3.09
ESLAM [9]	0.71	0.70	0.52	0.57	0.55	0.58	0.72	0.63	0.63
CoSLAM [35]	0.70	0.95	1.35	0.59	0.55	2.03	1.56	0.72	1.00
Ours	0.48	0.53	0.33	0.52	0.41	0.59	0.46	0.7	0.50

Table 2. Tracking ATE [cm] on TUM-RGBD [28]. Our method achieve a comparable performance among the neural vSLAMs. * denotes the reproduced results by running officially released code.

Method	#fr1/desk	#fr2/xyz	#fr3/office	#Avg.
DI-Fusion [7]	4.4	2.0	5.8	4.1
ElasticFusion [40]	2.5	1.2	2.5	2.1
BAD-SLAM [25]	1.7	1.1	1.7	1.5
Kintinous [39]	3.7	2.9	3.0	3.2
ORB-SLAM2 [16]	1.6	0.4	1.0	1.0
iMAP* [30]	7.2	2.12	9.0	6.1
NICE-SLAM [48]	4.3	31.7	3.9	13.3
Vox-Fusion* [42]	3.5	1.5	26.0	10.3
CoSLAM [35]	2.7	1.9	2.6	2.4
ESLAM [9]	2.3	1.1	2.4	2.0
Point-SLAM	2.6	1.3	3.2	2.4
Ours	3.3	1.3	6.6	3.7

LPIPS [46] by following [22]. To be fair, we run all the methods on a dataset 10 times and report the average results. More details can be found in the supplemental materials.

Implementation Details. GS-SLAM is implemented in Python using the PyTorch framework, incorporating CUDA code for Gaussian splatting and trained on a desktop PC with a 5.50GHz Intel Core i9-13900K CPU and NVIDIA RTX 4090 GPU. We extended the existing code for differentiable Gaussian splatting rasterization with additional functionality for handling depth, pose, and cumulative opacity during both forward and backward propagation. In all experiments, we set the learning rate of pose $\{\mathbf{R}, \mathbf{t}\}$ to 0.0002 and 0.0005, photometric loss weighting 0.8, geometric loss weighting 0.3, and keyframe window size $K = 10$. In the Replica dataset, we use 10 iterations for tracking and 100 iterations for mapping with max keyframe interval $\mu_k = 30$, while in the challenging TUM RGB-D dataset, we use 30 iterations for tracking, with max keyframe interval $\mu_k = 5$.

4.2. Evaluation of Localization and Mapping

Evaluation on Replica. Tracking ATE: Tab. 1 illustrates the **tracking performance** of our method and the state-of-the-art methods on the Replica dataset. Our method achieves the best or second performance in 7 of 8 scenes and outperforms the second-best method Point-SLAM [22] by 0.4 cm on average at 8.34 FPS. It is noticeable that the second best method, Point-SLAM [22] runs at 0.42 FPS, which is $20\times$ slower than our method, indicating that GS-SLAM achieve a better trade-off between the tracking accuracy and the runtime efficiency. **Mapping ACC:** Tab. 3 report the mapping evaluation results of our method with other current state-of-the-art visual SLAM methods. GS-SLAM

Table 3. Reconstruction comparison of the proposed method vs. the state-of-the-art methods on **Replica** dataset.

Method	Metric	Rm0	Rm1	Rm2	Off0	Off1	Off2	Off3	Off4	Avg.
NICESL	Depth L1 ↓	1.81	1.44	2.04	1.39	1.76	8.33	4.99	2.01	2.97
	Precision ↑	45.86	43.76	44.38	51.40	50.80	38.37	40.85	37.35	44.10
	Recall ↑	44.10	46.12	42.78	48.66	53.08	39.98	39.04	35.77	43.69
AM [48]	F1 ↑	44.96	44.84	43.56	49.99	51.91	39.16	39.92	36.54	43.86
	Depth L1 ↓	1.09	1.90	2.21	2.32	3.40	4.19	2.96	1.61	2.46
	Precision ↑	75.83	35.88	63.10	48.51	43.50	54.48	69.11	55.40	55.73
VoxFusion [42]	Recall ↑	64.89	33.07	56.62	44.76	38.44	47.85	60.61	46.79	49.13
	F1 ↑	69.93	34.38	59.67	46.54	40.81	50.95	64.56	50.72	52.20
	Depth L1 ↓	0.99	0.82	2.28	1.24	1.61	7.70	4.65	1.43	2.59
CoSLAM [35]	Precision ↑	81.71	77.95	73.30	79.41	80.67	55.64	57.63	79.76	73.26
	Recall ↑	74.03	70.79	65.73	71.46	70.35	52.96	56.06	71.22	66.58
	F1 ↑	77.68	74.20	69.31	75.23	75.16	54.27	56.83	75.25	69.74
ESLAM [9]	Depth L1 ↓	0.63	0.62	0.98	0.57	1.66	7.32	3.94	0.88	2.08
	Precision ↑	74.33	75.94	82.48	72.20	65.74	70.73	72.48	72.24	73.27
	Recall ↑	87.37	87.01	84.99	88.36	84.38	81.92	79.18	80.63	84.23
Ours	F1 ↑	80.32	81.10	83.72	79.47	73.90	75.92	75.68	76.21	78.29
	Depth L1 ↓	1.31	0.82	1.26	0.81	0.96	1.41	1.53	1.08	1.16
	Precision ↑	64.58	83.11	70.13	83.43	87.77	70.91	63.18	68.88	74.00
Ours	Recall ↑	61.29	76.83	63.84	76.90	76.15	61.63	62.91	61.50	67.63
	F1 ↑	62.89	79.85	66.84	80.03	81.55	65.95	59.17	64.98	70.15

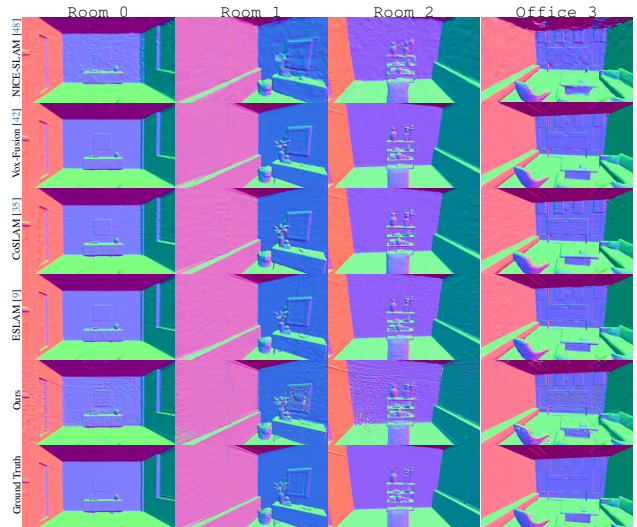


Figure 4. **Reconstruction** performance comparison of the proposed GS-SLAM and SOTA methods on the **Replica** dataset.

achieves the best performance in Depth L1 (1.16cm) and Precision (74.0%) metrics on average. For Recall and F1 scores, GS-SLAM performs comparably to the second best method CoSLAM [35]. The visualization results in Fig. 4 show that GS-SLAM achieves satisfying construction mesh with clear boundaries and details.

Evaluation on TUM-RGBD. Tab. 2 compares GS-SLAM with the other SLAM systems in TUM-RGBD dataset. Our method surpass iMAP [30], NICE-SLAM [48] and Vox-fusion [42], and achieve a comparable performance, average 3.7 cm ATE RSME, with the SOTA methods. A gap to traditional methods still exist between the neural vSLAM and the traditional SLAM systems, which employ more sophisticated tracking schemes [22].

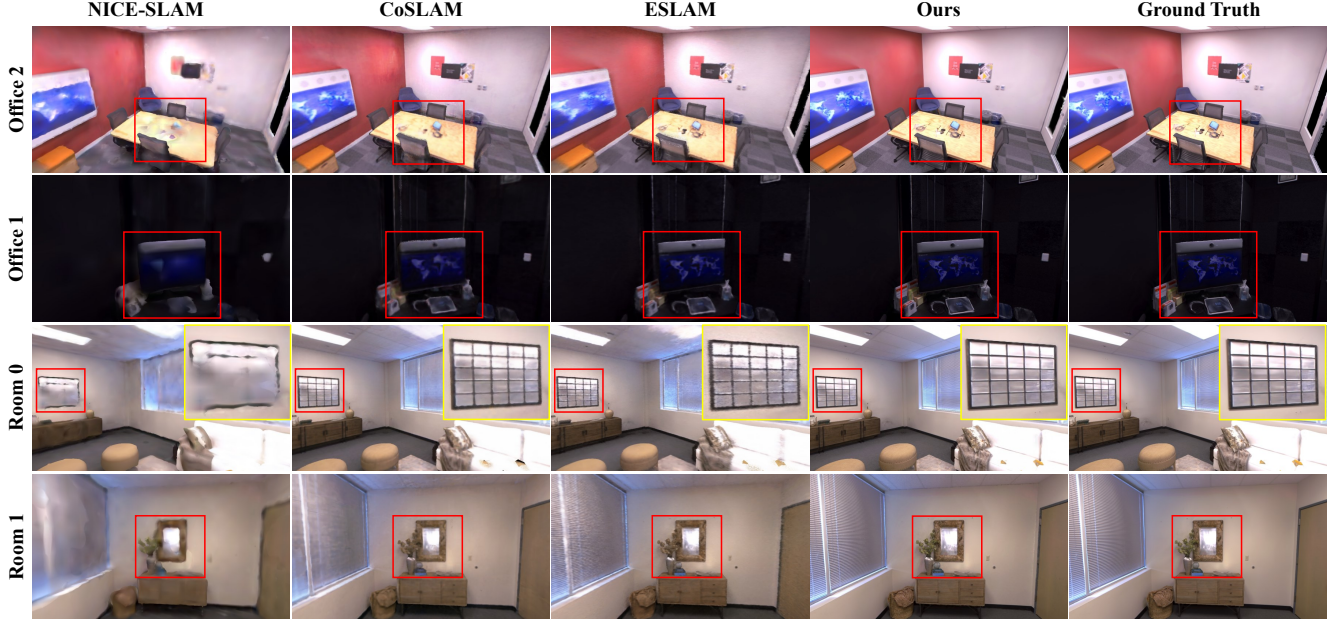


Figure 5. The render visualization results on the Replica dataset of the proposed GS-SLAM and state-of-the-art methods. GS-SLAM can generate much more high-quality and realistic images than the other methods, especially around the object boundaries.

Method	Metric	Room 0	Room 1	Room 2	Office 0	Office 1	Office 2	Office 3	Office 4	Avg.	FPS.
NICE-SLAM [48]	PSNR [dB] \uparrow	22.12	22.47	24.52	29.07	30.34	19.66	22.23	24.94	24.42	0.30
	SSIM \uparrow	0.689	0.757	0.814	0.874	0.886	0.797	0.801	0.856	0.809	
	LPIPS \downarrow	0.330	0.271	0.208	0.229	0.181	0.235	0.209	0.198	0.233	
Vox-Fusion* [42]	PSNR [dB] \uparrow	22.39	22.36	23.92	27.79	29.83	20.33	23.47	25.21	24.41	3.88
	SSIM \uparrow	0.683	0.751	0.798	0.857	0.876	0.794	0.803	0.847	0.801	
	LPIPS \downarrow	0.303	0.269	0.234	0.241	0.184	0.243	0.213	0.199	0.236	
CoSLAM [35]	PSNR [dB] \uparrow	27.27	28.45	29.06	34.14	34.87	28.43	28.76	30.91	30.24	3.68
	SSIM \uparrow	0.910	0.909	0.932	0.961	0.969	0.938	0.941	0.955	0.939	
	LPIPS \downarrow	0.324	0.294	0.266	0.209	0.196	0.258	0.229	0.236	0.252	
ESLAM [9]	PSNR [dB] \uparrow	25.32	27.77	29.08	33.71	30.20	28.09	28.77	29.71	29.08	2.82
	SSIM \uparrow	0.875	0.902	0.932	0.960	0.923	0.943	0.948	0.945	0.929	
	LPIPS \downarrow	0.313	0.298	0.248	0.184	0.228	0.241	0.196	0.204	0.336	
Ours	PSNR [dB] \uparrow	31.56	32.86	32.59	38.70	41.17	32.36	32.03	32.92	34.27	386.91
	SSIM \uparrow	0.968	0.973	0.971	0.986	0.993	0.978	0.970	0.968	0.975	
	LPIPS \downarrow	0.094	0.075	0.093	0.050	0.033	0.094	0.110	0.112	0.082	

Table 4. **Rendering Performance on Replica [26].** We outperform existing dense neural RGBD methods on the commonly reported rendering metrics. Note that GS-SLAM achieves 386 FPS on average, benefiting from the efficient Gaussian scene representation.

4.3. Rendering Evaluation

We compare the rendering performance of the proposed GS-SLAM with the neural visual SLAM methods in Tab. 4. The results show that GS-SLAM achieves the best performance in all the metrics. Our method significantly outperforms the second-best methods CoSLAM [35], ESLAM [9] and NICE-SLAM [48] by 1.52 dB in PSNR, 0.027 in SSIM and 0.12 in LPIPS, respectively. It is noticeable that GS-SLAM achieves 386 FPS rendering speed on average, which is 100 \times faster than the second-best method Vox-Fusion [42]. This excellent rendering performance is attributed to the efficient 3d Gaussian rendering pipeline and can be further applied to real-time downstream tasks, such as VR [4], robot navigation [6] and autonomous driving [2]. The visualization results in Fig. 5 show that GS-SLAM can generate

much more high-quality and realistic images than the other methods, especially in edge areas with detailed structures. While NICE-SLAM [48] causes severe artifacts and blurs, CoSLAM [35] and ESLAM [9] generate blur around the image boundaries.

4.4. Runtime Analysis

Tab. 5 illustrates the runtime and memory usage of GS-SLAM and the state-of-the-art methods on the Room 0 scene in the Replica dataset. We report the parameters of the neural networks and the memory usage of the scene representation. The results show that GS-SLAM achieves a competitive running speed with 8.34 FPS compared to the other Radiance Fields-based vSLAMs. Note that we do not use any neural network decoder in our system, which results in the zero learnable parameter. However, the 3D Gaussian

Table 5. **Runtime and Memory Usage on Replica Room 0.** The decoder parameters and embedding denote the parameter number of MLPs and the memory usage of the scene representation.

Method	Tracking [ms×it] ↓	Mapping [ms×it] ↓	System FPS ↑	Decoder param ↓	Scene Embedding ↓
Point-SLAM [22]	0.06 × 40	34.81 × 300	0.42	0.127 M	55.42 MB
NICE-SLAM [48]	6.64 × 10	28.63 × 60	2.91	0.06 M	48.48 MB
Vox-Fusion [42]	0.03 × 30	66.53 × 10	1.28	0.054 M	1.49 MB
CoSLAM [42]	6.01 × 10	13.18 × 10	16.64	1.671 M	—
ESLAM [42]	6.85 × 8	19.87 × 15	13.42	0.003 M	27.12 MB
GS-SLAM	11.9 × 10	12.8 × 100	8.34	0 M	198.04 MB

Table 6. **Ablation of the adaptive 3D Gaussian expansion strategy on #Room0 subset of the Replica Dataset.**

Setting	# Room0.							
	ATE ↓	Depth L1 ↓	Precision ↑	Recall ↑	F1 ↑	PSNR ↑	SSIM ↑	LPIPS ↓
w/o add	X	X	X	X	X	X	X	X
w/o delete	0.58	1.68	53.55	49.32	51.35	31.22	0.967	0.094
w/ add & delete	0.48	1.31	64.58	61.29	62.89	31.56	0.968	0.094

scene representations of GS-SLAM consume 198.04 MB memory, 4× larger than the second large method NICE-SLAM [48]. The memory usage is mainly caused by a large number of 3D Gaussian points in the scene representation for obtaining a detailed and dense map, which is a common constraint among Gaussian splatting-based 3D reconstruction methods. Despite this, we still achieve a 20 × faster FPS compared to the similar point-based method Point-SLAM [22].

4.5. Ablation Study

We perform the ablation of GS-SLAM on #Room0 of the Replica to evaluate the effectiveness of depth supervision, coarse to fine tracking, and expansion strategy for mapping. **Effect of our expansion strategy for mapping.** Tab. 6 shows the ablation of our proposed expansion strategy for mapping. The results illustrate that the expansion strategy can significantly improve the tracking and mapping performance. The implementation w/o adding means that we only initialize 3D Gaussian in the first frame and optimize the scene without adding new points. However, this strategy completely crashes because the density control in [11] can not handle real-time mapping tasks without an accurate point cloud input. Besides, the implementation w/o deletion suffers from a large number of redundant and noisy 3D Gaussian, which causes undesirable supervision. In contrast, the proposed expansion strategy effectively improves the tracking and mapping performance by 0.1 in ATE and 11.97 in Recall by adding more accurate constraints for the optimization. According to the visualization results in Fig. 6, our full implementation achieves more high-quality and detailed rendering and reconstruction results than the w/o delete strategy.

Effect of depth supervision. Tab. 7 illustrates quantitative evaluation using depth supervision in mapping. In contrast to the original color-only supervision in [11], the depth supervision can significantly improve the tracking

Table 7. **Depth supervision ablation on #Room0 of Replica.**

Setting	# Room0.							
	ATE ↓	Depth L1 ↓	Precision ↑	Recall ↑	F1 ↑	PSNR ↑	SSIM ↑	LPIPS ↓
w/o Depth	0.80	3.21	14.28	15.01	14.63	29.76	0.956	0.107
w/ Depth	0.48	1.31	64.58	61.29	62.89	31.56	0.968	0.094

Table 8. **Ablation of the coarse to fine tracking strategy on #Room0 subset of the Replica dataset.**

Setting	# Room0.							
	ATE ↓	Depth L1 ↓	Precision ↑	Recall ↑	F1 ↑	PSNR ↑	SSIM ↑	LPIPS ↓
Coarse	0.91	1.48	59.68	57.54	56.50	29.13	0.954	0.120
Fine	0.49	1.39	62.61	59.18	61.29	30.84	0.964	0.096
Coarse to fine	0.48	1.31	64.58	61.29	62.89	31.56	0.968	0.094

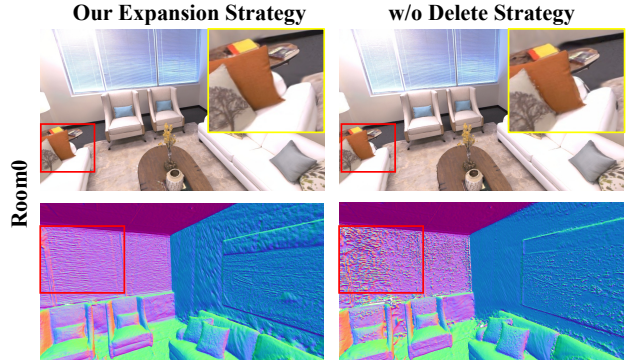


Figure 6. Rendering and mesh visualization of the **adaptive 3D Gaussian expansion ablation** on #Room0 subset of Replica.

and mapping performance by providing accurate geometry constraints for the optimization. Our implementation with depth achieves better tracking ATE of 0.48, mapping precision of 64.58, and rendering PSNR of 31.56 compared with the implementation without depth supervision.

Effect of coarse to fine tracking. According to the results in Tab. 8, the proposed coarse-to-fine tracking strategy performs best in all tracking, mapping, and rendering metrics. Compared with fine tracking, the coarse to fine tracking strategy significantly improves the performance by 0.01 in tracking ATE, 2.11 in Recall, and 0.72 in PSNR. Although the fine strategy surpasses the coarse strategy in precision, it suffers from the artifacts and noise in the reconstructed scene, leading to a fluctuation optimization. The coarse-to-fine strategy effectively avoids noise reconstruction and improves accuracy and robustness.

5. Conclusion and Limitations

We presented GS-SLAM, a dense visual SLAM approach that takes advantage of fast and high-quality rendering superiorities of 3D Gaussian Splatting. The proposed adaptive 3D Gaussian expansion strategy and coarse-to-fine camera tracking technique enable GS-SLAM to dynamically reconstruct detailed, dense maps and effectively produce a robust camera pose estimation. We demonstrated GS-SLAM through extensive experiments that our approach achieves competitive performance in both reconstruction and localization with much lower time consumption, resulting in a

better balance between running speed and accuracy.

Limitations. Our method relies on the depth sensor reading to initialize and update 3D Gaussians. In environments where high-quality depth information is unavailable, the effectiveness of this system may be compromised. We believe a better optimization method can be designed to update the initial 3D Gaussian position on the fly. Also, our method has a high memory usage when applied to large-scale scenes, and we hope to address this problem in future work via incorporating neural scene representations.

References

- [1] Michael Bloesch, Jan Czarnowski, Ronald Clark, Stefan Leutenegger, and Andrew J. Davison. Codeslam - learning a compact, optimisable representation for dense visual slam. *2018 IEEE/CVF Conference on Computer Vision and Pattern Recognition*, pages 2560–2568, 2018. [2](#)
- [2] Guillaume Bresson, Zayed Alsayed, Li Yu, and Sébastien Glaser. Simultaneous localization and mapping: A survey of current trends in autonomous driving. *IEEE Transactions on Intelligent Vehicles*, 2:194–220, 2017. [7](#)
- [3] Zilong Chen, Feng Wang, and Huaping Liu. Text-to-3d using gaussian splatting. *ArXiv*, abs/2309.16585, 2023. [3](#)
- [4] Parth Rajesh Desai, Pooja Nikhil Desai, Komal Deepak Ajmera, and Khushbu Mehta. A review paper on oculus rift-a virtual reality headset. *ArXiv*, abs/1408.1173, 2014. [7](#)
- [5] Hugh F. Durrant-Whyte and Tim Bailey. Simultaneous localization and mapping: part i. *IEEE Robotics & Automation Magazine*, 13:99–110, 2006. [1](#)
- [6] Christian Häne, Christopher Zach, Jongwoo Lim, Ananth Ranganathan, and Marc Pollefeys. Stereo depth map fusion for robot navigation. *2011 IEEE/RSJ International Conference on Intelligent Robots and Systems*, pages 1618–1625, 2011. [7](#)
- [7] Jiahui Huang, Shi-Sheng Huang, Haoxuan Song, and Shi-Min Hu. Di-fusion: Online implicit 3d reconstruction with deep priors. In *IEEE/CVF Conference on Computer Vision and Pattern Recognition*, pages 8932–8941, 2021. [6](#)
- [8] Xudong Jiang, Lifeng Zhu, Jia Liu, and Aiguo Song. A slam-based 6dof controller with smooth auto-calibration for virtual reality. *The Visual Computer*, 39:3873 – 3886, 2022. [1](#)
- [9] Mohammad Mahdi Johari, Camilla Carta, and Franccois Fleuret. Eslam: Efficient dense slam system based on hybrid representation of signed distance fields. *CVPR*, 2023. [1](#), [2](#), [5](#), [6](#), [7](#)
- [10] Olaf Kähler, Victor Adrian Prisacariu, Julien P. C. Valentin, and David William Murray. Hierarchical voxel block hashing for efficient integration of depth images. *IEEE Robotics and Automation Letters*, 1:192–197, 2016. [1](#)
- [11] Bernhard Kerbl, Georgios Kopanas, Thomas Leimkühler, and George Drettakis. 3d gaussian splatting for real-time radiance field rendering. *ACM Transactions on Graphics*, 42(4), 2023. [2](#), [3](#), [8](#)
- [12] Georg S. W. Klein and David William Murray. Parallel tracking and mapping on a camera phone. *2009 8th IEEE International Symposium on Mixed and Augmented Reality*, pages 83–86, 2009. [2](#)
- [13] Jonathon Luiten, Georgios Kopanas, Bastian Leibe, and Deva Ramanan. Dynamic 3d gaussians: Tracking by persistent dynamic view synthesis. *ArXiv*, abs/2308.09713, 2023. [2](#), [3](#)
- [14] Robert Maier, Raphael Schaller, and Daniel Cremers. Efficient online surface correction for real-time large-scale 3d reconstruction. *ArXiv*, abs/1709.03763, 2017. [1](#)
- [15] Ben Mildenhall, Pratul P. Srinivasan, Matthew Tancik, Jonathan T. Barron, Ravi Ramamoorthi, and Ren Ng. Nerf: Representing scenes as neural radiance fields for view synthesis. In *ECCV*, 2020. [1](#)
- [16] Raul Mur-Artal and Juan D. Tardós. Orb-slam2: An open-source slam system for monocular, stereo, and rgb-d cameras. *IEEE Transactions on Robotics*, 33:1255–1262, 2016. [1](#), [6](#)
- [17] Richard A. Newcombe, Shahram Izadi, Otmar Hilliges, David Molyneaux, David Kim, Andrew J. Davison, Pushmeet Kohli, Jamie Shotton, Steve Hodges, and Andrew William Fitzgibbon. Kinectfusion: Real-time dense surface mapping and tracking. *2011 10th IEEE International Symposium on Mixed and Augmented Reality*, pages 127–136, 2011. [1](#)
- [18] Richard A. Newcombe, S. Lovegrove, and Andrew J. Davison. Dtam: Dense tracking and mapping in real-time. *ICCV*, pages 2320–2327, 2011. [2](#)
- [19] Matthias Nießner, Michael Zollhöfer, Shahram Izadi, and Marc Stamminger. Real-time 3d reconstruction at scale using voxel hashing. *ACM Transactions on Graphics (TOG)*, 32:1 – 11, 2013. [1](#)
- [20] Gerhard Reitmayr, Tobias Langlotz, Daniel Wagner, Alessandro Mulloni, Gerhard Schall, Dieter Schmalstieg, and Qi Pan. Simultaneous localization and mapping for augmented reality. *2010 International Symposium on Ubiquitous Virtual Reality*, pages 5–8, 2010. [1](#)
- [21] Fabio Ruetz, Emili Hernández, Mark Pfeiffer, Helen Oleynikova, Mark Cox, Thomas Lowe, and Paulo Viniçius Koerich Borges. Ovpv mesh: 3d free-space representation for local ground vehicle navigation. *2019 International Conference on Robotics and Automation (ICRA)*, pages 8648–8654, 2018. [1](#)
- [22] Erik Sandström, Yue Li, Luc Van Gool, and Martin R. Oswald. Point-slam: Dense neural point cloud-based slam. In *ICCV*, 2023. [2](#), [5](#), [6](#), [8](#)
- [23] Johannes Lutz Schönberger and Jan-Michael Frahm. Structure-from-motion revisited. In *Conference on Computer Vision and Pattern Recognition (CVPR)*, 2016. [3](#)
- [24] Thomas Schöps, Torsten Sattler, and Marc Pollefeys. Bad slam: Bundle adjusted direct rgb-d slam. *2019 IEEE/CVF Conference on Computer Vision and Pattern Recognition (CVPR)*, pages 134–144, 2019. [2](#)
- [25] Thomas Schöps, Torsten Sattler, and Marc Pollefeys. BAD SLAM: Bundle adjusted direct RGB-D SLAM. In *CVF/IEEE Conference on Computer Vision and Pattern Recognition (CVPR)*, 2019. [6](#)

- [26] Julian Straub, Thomas Whelan, Lingni Ma, Yufan Chen, Erik Wijmans, Simon Green, Jakob J. Engel, Raul Mur-Artal, Carl Yuheng Ren, Shobhit Verma, Anton Clarkson, Ming Yan, Brian Budge, Yajie Yan, Xiaqing Pan, June Yon, Yuyang Zou, Kimberly Leon, Nigel Carter, Jesus Briales, Tyler Gillingham, Elias Mueggler, Luis Pesqueira, Manolis Savva, Dhruv Batra, Hauke Malte Strasdat, Renzo De Nardi, Michael Goesele, S. Lovegrove, and Richard A. Newcombe. The replica dataset: A digital replica of indoor spaces. *ArXiv*, abs/1906.05797, 2019. 5, 7
- [27] J. Stückler and Sven Behnke. Multi-resolution surfel maps for efficient dense 3d modeling and tracking. *J. Vis. Commun. Image Represent.*, 25:137–147, 2014. 1
- [28] Jürgen Sturm, Nikolas Engelhard, Felix Endres, Wolfram Burgard, and Daniel Cremers. A benchmark for the evaluation of RGB-D SLAM systems. In *International Conference on Intelligent Robots and Systems (IROS)*. IEEE/RSJ, 2012. 5, 6
- [29] Edgar Sucar, Kentaro Wada, and Andrew J. Davison. Nodestlam: Neural object descriptors for multi-view shape reconstruction. *2020 International Conference on 3D Vision (3DV)*, pages 949–958, 2020. 2
- [30] Edgar Sucar, Shikun Liu, Joseph Ortiz, and Andrew J. Davison. imap: Implicit mapping and positioning in real-time. *ICCV*, 2021. 1, 2, 5, 6
- [31] Jiaxiang Tang, Jiawei Ren, Hang Zhou, Ziwei Liu, and Gang Zeng. Dreamgaussian: Generative gaussian splatting for efficient 3d content creation. *ArXiv*, abs/2309.16653, 2023. 3
- [32] Zachary Teed and Jia Deng. Droid-slam: Deep visual slam for monocular, stereo, and rgb-d cameras. In *Neural Information Processing Systems*, 2021. 2
- [33] Andreas Langeland Teigen, Yeonsoo Park, Annette Stahl, and Rudolf Mester. Rgb-d mapping and tracking in a plenoxel radiance field. *ArXiv*, abs/2307.03404, 2023. 2
- [34] Charalambos Theodorou, Vladan Velisavljevic, Vladimir Dyo, and Fredi Nonyelu. Visual slam algorithms and their application for ar, mapping, localization and wayfinding. *Arxiv*, 15:100222, 2022. 1
- [35] Hengyi Wang, Jingwen Wang, and Lourdes de Agapito. Coslam: Joint coordinate and sparse parametric encodings for neural real-time slam. *CVPR*, 2023. 1, 5, 6, 7
- [36] Kaixuan Wang, Fei Gao, and Shaojie Shen. Real-time scalable dense surfel mapping. *2019 International Conference on Robotics and Automation (ICRA)*, pages 6919–6925, 2019. 1
- [37] Zhou Wang, Alan C Bovik, Hamid R Sheikh, and Eero P Simoncelli. Image quality assessment: from error visibility to structural similarity. *IEEE transactions on image processing*, 13(4):600–612, 2004. 5
- [38] Thomas Whelan, Michael Kaess, Maurice F. Fallon, Hordur Johannsson, John J. Leonard, and John B. McDonald. Kintinuous: Spatially extended kinectfusion. In *AAAI*, 2012. 2
- [39] Thomas Whelan, John McDonald, Michael Kaess, Maurice Fallon, Hordur Johannsson, and John J. Leonard. Kintinuous: Spatially extended kinectfusion. In *Proceedings of RSS '12 Workshop on RGB-D: Advanced Reasoning with Depth Cameras*, 2012. 6
- [40] Thomas Whelan, Stefan Leutenegger, Renato Salas-Moreno, Ben Glocker, and Andrew Davison. Elasticfusion: Dense slam without a pose graph. In *Robotics: Science and Systems (RSS)*, 2015. 1, 6
- [41] Guanjun Wu, Taoran Yi, Jiemin Fang, Lingxi Xie, Xiaopeng Zhang, Wei Wei, Wenyu Liu, Qi Tian, and Xinggang Wang. 4d gaussian splatting for real-time dynamic scene rendering. *ArXiv*, abs/2310.08528, 2023. 2, 3
- [42] Xingrui Yang, Hai Li, Hongjia Zhai, Yuhang Ming, Yuqian Liu, and Guofeng Zhang. Vox-fusion: Dense tracking and mapping with voxel-based neural implicit representation. *2022 IEEE International Symposium on Mixed and Augmented Reality (ISMAR)*, pages 499–507, 2022. 2, 5, 6, 7, 8
- [43] Ziyi Yang, Xinyu Gao, Wenming Zhou, Shaohui Jiao, Yuqing Zhang, and Xiaogang Jin. Deformable 3d gaussians for high-fidelity monocular dynamic scene reconstruction. *ArXiv*, abs/2309.13101, 2023. 3
- [44] Zeyu Yang, Hongye Yang, Zijie Pan, Xiatian Zhu, and Li Zhang. Real-time photorealistic dynamic scene representation and rendering with 4d gaussian splatting. *ArXiv*, abs/2310.10642, 2023. 2
- [45] Taoran Yi, Jiemin Fang, Guanjun Wu, Lingxi Xie, Xiaopeng Zhang, Wenyu Liu, Qi Tian, and Xinggang Wang. Gaussian-dreamer: Fast generation from text to 3d gaussian splatting with point cloud priors. *ArXiv*, abs/2310.08529, 2023. 3
- [46] Richard Zhang, Phillip Isola, Alexei A Efros, Eli Shechtman, and Oliver Wang. The unreasonable effectiveness of deep features as a perceptual metric. In *IEEE conference on computer vision and pattern recognition*, pages 586–595, 2018. 6
- [47] Shuaifeng Zhi, Michael Bloesch, Stefan Leutenegger, and Andrew J. Davison. Scenecode: Monocular dense semantic reconstruction using learned encoded scene representations. *2019 IEEE/CVF Conference on Computer Vision and Pattern Recognition (CVPR)*, pages 11768–11777, 2019. 2
- [48] Zihan Zhu, Songyou Peng, Viktor Larsson, Weiwei Xu, Hujun Bao, Zhaopeng Cui, Martin R. Oswald, and Marc Pollefeys. Nice-slam: Neural implicit scalable encoding for slam. *CVPR*, 2021. 1, 2, 5, 6, 7, 8
- [49] Wojciech Zielonka, Timur M. Bagautdinov, Shunsuke Saito, Michael Zollhofer, Justus Thies, and Javier Romero. Drivable 3d gaussian avatars. 2023. 3
- [50] Matthias Zwicker, Hanspeter Pfister, Jeroen van Baar, and Markus H. Gross. Ewa volume splatting. *Proceedings Visualization, 2001. VIS '01.*, pages 29–538, 2001. 3